RESEARCH ARTICLE
SOLID EARTH: SEISMOLOGY

Earth and Planetary Physics
8: 811–821, 2024
doi: 10.26464/epp2024041

The existence of saturated vapors in the deep source region of 2017 Pohang earthquake evidenced from seismic tomography

JiaWei Qian[1,2], HaiJiang Zhang[3*], Lei Guo[4], Uzonna Okenna Anyiam[5], Changsoo Cho[6], Kang Hyeun Ji[6], and HaoRan Ma[2]

[1]School of Carbon Neutrality Science and Engineering, Anhui University of Science and Technology, Hefei 231131, China;

[2]College of Oceanography, Hohai University, Nanjing 210098, China;

[3]Laboratory of Seismology and Physics of Earth's Interior, School of Earth and Space Sciences, University of Science and Technology of China, Hefei 230026, China;

[4]Hebei Earthquake Agency, Shijiazhuang 050022, China;

[5]Geological and Environmental Science, Hope College, Holland, MI 49423, US;

[6]Earthquake Research Center, Korea Institute of Geoscience and Mineral Resources, Daejeon 34132, Korea

Key Points:

- Three-dimensional velocity images of V_p, V_s, and V_p/V_s are estimated for the source area of the 2017 Pohang M_w5.5 earthquake.
- Low V_p, high V_s, and low V_p/V_s anomalies are imaged in the deep source area that are related to overpressurized vapors.
- The 2017 Pohang earthquake is initiated around the edge of the low V_p/V_s area where most of aftershocks are located.

Citation: Qian, J. W., Zhang, H. J., Guo, L., Anyiam, U. O., Cho, C., Ji, K. H., and Ma, H. R. (2024). The existence of saturated vapors in the deep source region of 2017 Pohang earthquake evidenced from seismic tomography. *Earth Planet. Phys.*, *8*(5), 811–821. http://doi.org/10.26464/epp2024041

Abstract: Geothermal resources are a promising approach to clean renewable energy; 90% of them are deep reservoirs of hot dry rock that require hydraulic fracturing to create a network of connections among wells to enable efficient heat exchange, known as an Enhanced Geothermal System (EGS). The Pohang EGS project in south Korea led to a devasting M_w5.5 earthquake, triggered by the reservoir's EGS stimulation, the largest earthquake known to have been induced by EGS development. Detailed investigations have been conducted to understand the cause of the Pohang earthquake; the conclusion has been that overpressurized injected fluids migrated into an unknown fault triggering this large earthquake. Detailed velocity images for the source zone of the 2017 Pohang earthquake, which could be helpful for further understanding its inducing mechanism, are unavailable. However, we have assembled detailed aftershock data recorded by 41 local stations installed within about three months after the M_w5.5 Pohang earthquake, and have then applied the V_p/V_s model's consistency-constrained double-difference seismic tomography method to determine the high-resolution three-dimensional V_p (compressional wave velocity), V_s (shear wave velocity), and V_p/V_s models of the source region that we report here, as well as earthquake locations within the source region. The velocity images reveal that the deep source area of the 2017 Pohang earthquake is dominated by low V_p, high V_s, and low V_p/V_s anomalies, a pattern that can be caused by overpressurized vapors due to high temperatures at these depths. Based on aftershock locations and velocity features, our studies support the conclusion that the 2017 Pohang earthquake was triggered by injected EGS fluids that migrated into a blind fault.

Keywords: Pohang earthquake; tomoDDMC; low V_p/V_s; saturated vapors; EGS

1. Introduction

Potential sources of geothermal energy, which is renewable and sustainable, are widely distributed on the Earth (Lu SM, 2018; Anderson and Rezaie, 2019; Liu HY, 2022). Compared to conventional hydrothermal resources, hot dry rock (HDR) resources at a depth of 3-10 km that contain little or no water account for 90% of global geothermal resources (Olasolo et al., 2016; Yin XX et al., 2021). To exploit an HDR resource, an Enhanced Geothermal System (EGS) must be constructed to increase the permeability of the reservoir so that fluids can flow between injection and production wells (Yoo et al., 2021). However, EGS development involves hydraulic stimulation that may induce damaging earthquakes such as the moderate *M*2.9 earthquake at the geothermal site of Soultz-sous-Forêts (Charléty et al., 2007) the M_L3.4 earthquake at the geothermal site in Basel, Switzerland (Häring et al., 2008), and particularly the large M_w5.5 earthquake in 2017 that occurred near an EGS drilling site in Pohang, Republic of Korea (Kim et al., 2018; Grigoli et al., 2018; Lee et al., 2019).

First author: J. W. Qian, qianjw@hhu.edu.cn
Correspondence to: H. J. Zhang, zhang11@ustc.edu.cn
Received 27 DEC 2023; Accepted 04 JUN 2024.
First Published online 19 JUL 2024.

In general, three mechanisms have been proposed to explain the induced seismicity due to hydraulic fracturing, including fluid pressure diffusion (Lei XL et al., 2019; Wong et al., 2021), poro-thermoelastic effects (Ellsworth, 2013), and aseismic fault slip (Bhattacharya and Viesca, 2019). Seismicity induced by hydraulic fracturing in EGS projects is more dangerous than in the hydrocarbon industry because fluid injection in crystalline rocks tends to be more seismogenic than in the sedimentary rocks associated with petroleum and natural gas extraction (Evans et al., 2012).

The 2017 Pohang M_w5.5 earthquake is so far the largest induced earthquake due to EGS development, and has been studied by various methods (Kim et al., 2018; Grigoli et al., 2018; Ellsworth et al., 2019; Terakawa et al., 2020; Yeo et al., 2020). Geological and geophysical data analyzed by Kim et al. (2018) suggested that the Pohang earthquake was induced by fluids from the EGS site. Grigoli et al. (2018) combined seismological and geodetic analyses to infer that the occurrence of this earthquake was influenced by the injection operations at the nearby EGS site. Ellsworth et al. (2019) comprehensively examined the tectonic stress conditions, local geology, well drilling data, and well stimulation data, and the seismicity induced by injection, and concluded that the 2017 Pohang earthquake was triggered by high-pressure injection into the EGS well that sent fluid into a previously unmapped fault. Choi et al. (2019) provided insights into the source mechanism of the 2017 Pohang earthquake, relating it to reverse reactivations of pre-existing normal faults. Yeo et al. (2020) proposed a multifaceted causal mechanism, using detailed data from the EGS hydraulic stimulation and related on-site seismicity monitoring data. Using aftershock data recorded by a dense regional portable seismic array from 10 November 2017 to 20 October 2018, Kim et al. (2020) applied the double-difference location method (hypoDD) developed by Waldhauser and Ellsworth (2000) to obtain a relative earthquake location of the Pohang earthquake sequence. Terakawa et al. (2020) used focal mechanism tomography to estimate the 3-D pore fluid pressure field in the source region of the 2017 Pohang earthquake.

However, a detailed velocity model of the 2017 Pohang earthquake source region is so far unavailable, and the fluid state causing high pore pressures in the source region is unknown. Accurate information on the 3D velocity structure in the source area is important to understand the seismogenic environment and the mechanism of this and other induced earthquakes. Seismic velocity anomalies in source regions have helped to track fluid migration and thus identify likely inducing mechanisms for earthquakes in shale gas development areas (Tan YY et al., 2020, 2023). Concha et al. (2010) used the double-difference tomography method (tomoDD) to image the V_p and V_s of the European HDR geothermal reservoir at Soultz-sous-Forets in order to understand the fluid path. Compared to separate V_p and V_s models, the V_p/V_s model is more sensitivity to fluids and fractures (Christensen, 1996; Takei, 2002). Lin GQ and Wu B (2018) found low V_p/V_s anomalies in the Geysers Geothermal Field using the simul2000 algorithm; these anomalies suggest the existence of vapors. In this study our goal is to resolve fine velocity structures of the source region of the 2017 Pohang earthquake by applying the V_p/V_s model's consistency-constrained double-difference seismic tomography method to a significant quantity of aftershock data (Guo H et al., 2018). This approach is expected to increase significantly the resolution and reliability of the V_p/V_s model.

2. Seismic Data

The Pohang EGS project was intended to develop geothermal energy in a ~4 km deep hot granitic reservoir. Above the granitic reservoir, the strata from deep to shallow in this area are Quaternary sediments, Tertiary volcanic and sedimentary rocks, and Cretaceous volcanic and sedimentary rocks, respectively (Ellsworth et al., 2019). Over the course of approximately four years, from 2012 to 2016, two exploratory wells named PX-1 and PX-2 were drilled into the granitic basement to develop the EGS. PX-1 and PX-2 are six meters apart from each other in the north-south direction on the surface and are about 600 m apart at the bottom (Figure 1b).

Five hydraulic stimulations were conducted between 29 January 2016 and 18 September 2017. The first, third, and fifth stimulations were conducted in PX-2 and the second and fourth in PX-1. The Pohang earthquake occurred approximately two months after the completion of the final stimulation. In total, more than 5800 m^3 of hydraulic fracturing fluid were not recovered after the stimulations (Ellsworth et al., 2019; Terakawa et al., 2020). A volume of fluid this large can play an important role in triggering an induced earthquake, especially via the mechanism of fluid pressure diffusion (Bhattacharya and Viesca, 2019; Terakawa et al., 2020).

For this study, we use seismic phase arrival times of 1124 aftershocks of the 2017 Pohang earthquake, recorded by 41 stations (Figure 1a), collected by the Korea Institute of Geoscience and Mineral Resources (KIGAM). The earthquake magnitudes (Figure 2) were determined by Kim et al. (2020). Seismicity remained at a high level for about three months, but especially during the first 20 days after the mainshock (Figure 2).

3. Seismic Tomographic Method

Zhang HJ and Thurber (2003) developed the original double-difference seismic tomography algorithm (tomoDD) to simultaneously invert velocity structure and event locations. The V_p/V_s model could be directly derived by dividing V_p by V_s. However, because V_p and V_s models generally have different model resolutions and uncertainties, V_p/V_s models obtained simply by dividing V_p by V_s inevitably suffer from artifacts (Thurber, 1993; Zhang HJ et al., 2009). In order to obtain a more reliable V_p/V_s model, Zhang HJ et al. (2009) made use of absolute and differential P, S, and S-P times to jointly invert earthquake locations as well as V_p, V_s, and V_p/V_s models. On this basis, Guo H et al. (2018) proposed the consistency-constrained double-difference seismic tomography method, creating a more reliable V_p/V_s model that has a resolution similar to those of the separate V_p and V_s models.

Assume that k_1 and k_2 represent the V_p/V_s model obtained by dividing V_p by V_s and by inverting S-P data, respectively. The difference between k_1 and k_2 is defined as

$$\Delta = k_1 - k_2 = \frac{u_s}{u_p} - k_2, \tag{1}$$

where u_p and u_s represent the slowness of the P and S waves, respectively. In an ideal case, the difference should be zero; thus

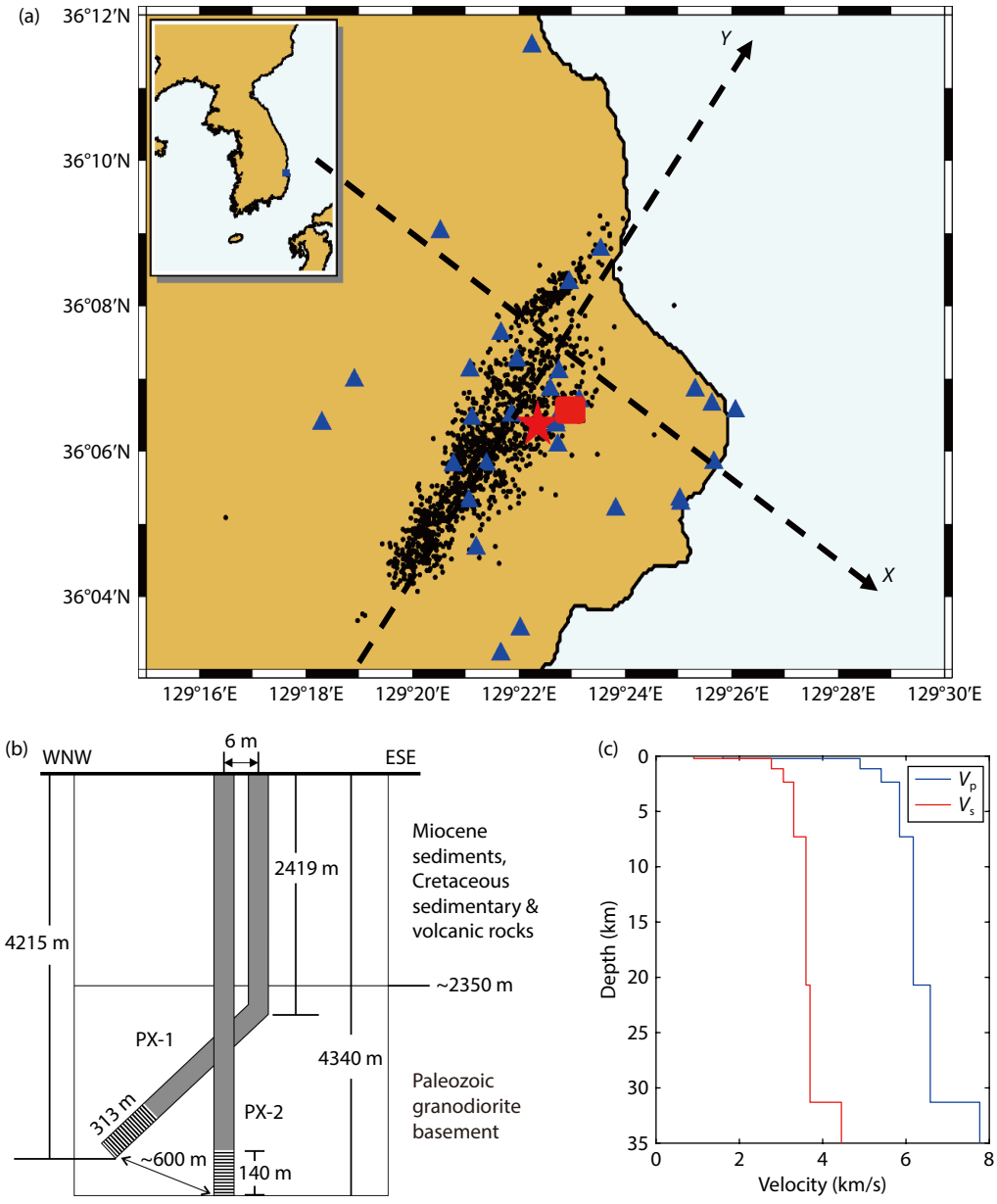

Figure 1. (a) Horizontal distribution of the aftershocks (black dots), the seismic stations (blue triangles), the mainshock (red star), and the wells (red square). (b) The schematics of the two exploration wells PX-1 and PX-2 (from Geological Society of Korea). (c) 1-D initial velocity model of V_p and V_s.

we can obtain a reliable and high-resolution V_p/V_s model by minimizing the difference between two V_p/V_s models, as follows (Guo H et al., 2018):

$$\begin{aligned} d\Delta &= \Delta^{\text{ture}} - \Delta^{\text{cal}} = k_2 - \frac{u_s}{u_p} \\ &= \frac{\partial \Delta}{\partial u_p}\delta u_p + \frac{\partial \Delta}{\partial u_s}\delta u_s + \frac{\partial \Delta}{\partial k_2}\delta k_2 \\ &= -\frac{u_s}{u_p^2}\delta u_p + \frac{1}{u_p}\delta u_s - \delta k_2 . \end{aligned} \tag{2}$$

The V_p/V_s model consistency constraint in Equation (2) can be combined with the double-difference seismic tomography system of Zhang HJ et al. (2009) to better determine V_p, V_s, and V_p/V_s models. This method has been widely used to obtain high-resolution V_p/V_s models for different regions (Guo H et al., 2018; Zuo KZ et al., 2020; Anyiam et al., 2023; Cao Y et al., 2023; Tan YY et al., 2023).

4. Tomographic Details and Results

Here we apply the consistency-constrained double-difference seismic tomography method (Guo H et al., 2018) to obtain 3D V_p, V_s, and V_p/V_s models in the source region of the 2017 Pohang earthquake. Figure 1a shows the Cartesian coordinate system used for the inversion. The location of the EGS site was selected as the coordinate origin. The grid nodes in the depth direction are positioned at Z = 0, 0.21, 1.14, 2.35, 3, 4, 5, 6, 7.29, 10, 12, 20.7, 25, and 31.3 km, respectively. The vertical grid was set referring to local strata. Note that the depth of Z = 0 km represents the depth of mean sea level. Along the X and Y directions, the grid intervals are set as 1 km away from the source region and 0.5 km in the

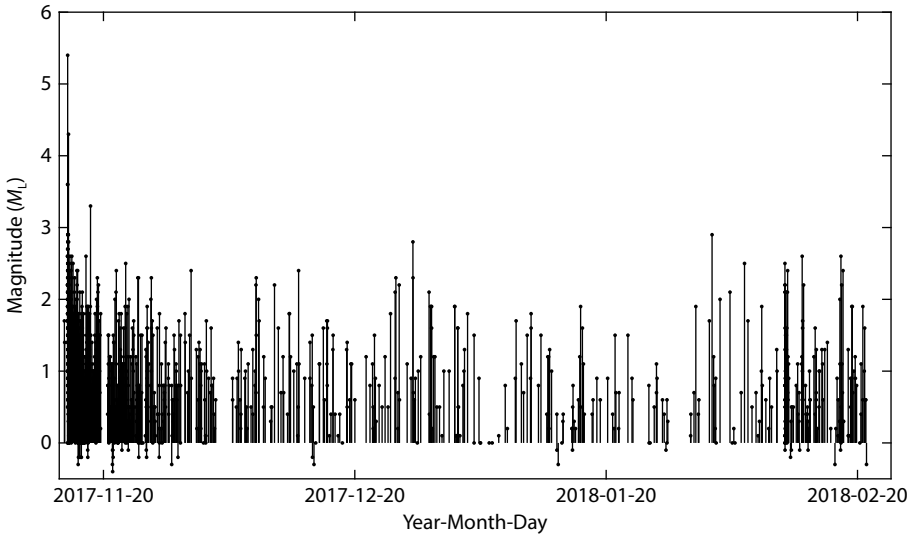

Figure 2. Time-magnitude distribution of the Pohang earthquake sequence.

source region. Figure 1c presents the initial one-dimensional V_p and V_s models for the inversion based on the regional velocity model for earthquake monitoring.

For seismic phase arrivals, we assembled 3281 P-wave, 2003 S-wave, and 1377 S-P absolute arrival times, from which differential arrival times can be constructed for event pairs when interevent distances are smaller than 5 km and the number of neighbors is smaller than 8. In total, 29,686 P-wave and S-wave relative arrival times, and 6441 S-P relative arrival times, were constructed. The average offset between event pairs is 0.47 km. After a total of 32 iterations, the root-mean-square (RMS) travel time residual decreased from 0.060 s to 0.019 s. The travel time residuals after inversion were more concentrated than those before inversion, indicating that the final velocity models better fit the data than the initial model (Figure 3).

To assess the model's resolution, we performed a checkerboard resolution test similar to previous studies (Guo H et al., 2018; Zuo KZ et al., 2020; Anyiam et al., 2023; Cao Y et al., 2023). We created synthetic velocity models based on the 1-D initial model with ±5% perturbations on neighboring grid nodes. V_p and V_s perturbations have opposite signs so that the V_p/V_s model also has checkerboard patterns with anomalies of +10.5% and −9.5% on adjacent grid

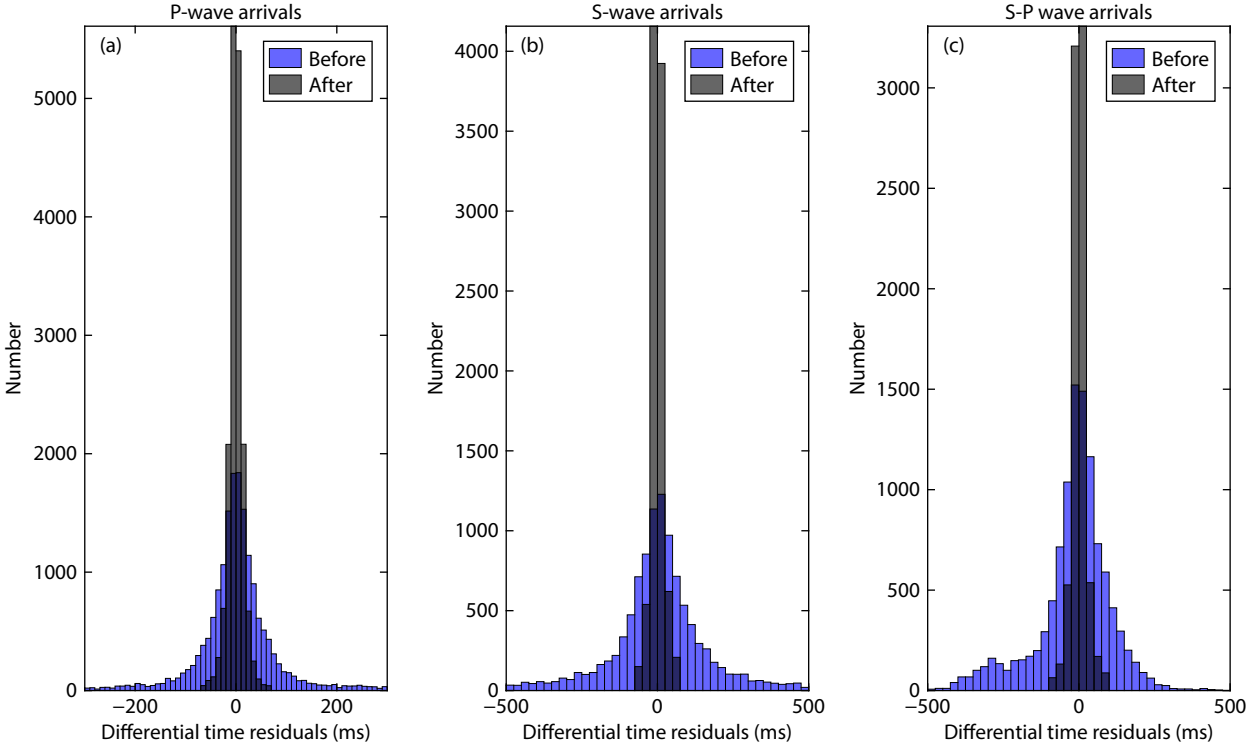

Figure 3. Histograms of travel time residuals. Residual histogram after the inversion (grey) is superimposed on residual histogram before the inversion (blue). (a) P-wave arrivals. (b) S-wave arrivals. (c) S-P wave arrivals.

nodes. Based on the synthetic model, theoretical travel times were generated through a pseudo-bending ray-tracing algorithm (Zhang HJ and Thurber, 2003) with the same data distribution as the real data. Finally, the synthetic data were inverted using the same inversion strategy as that of the real inversion.

The two exploratory wells, PX-1 and PX-2, are located near X = 0 km and Y = 0 km, respectively. Figure 4 shows vertical profiles of recovered V_P, V_S, and V_P/V_S checkerboard models along or across the earthquake clusters at X = 0 km and Y = 0 km, respectively. Figure 5b shows the recovered checkerboard results at depths

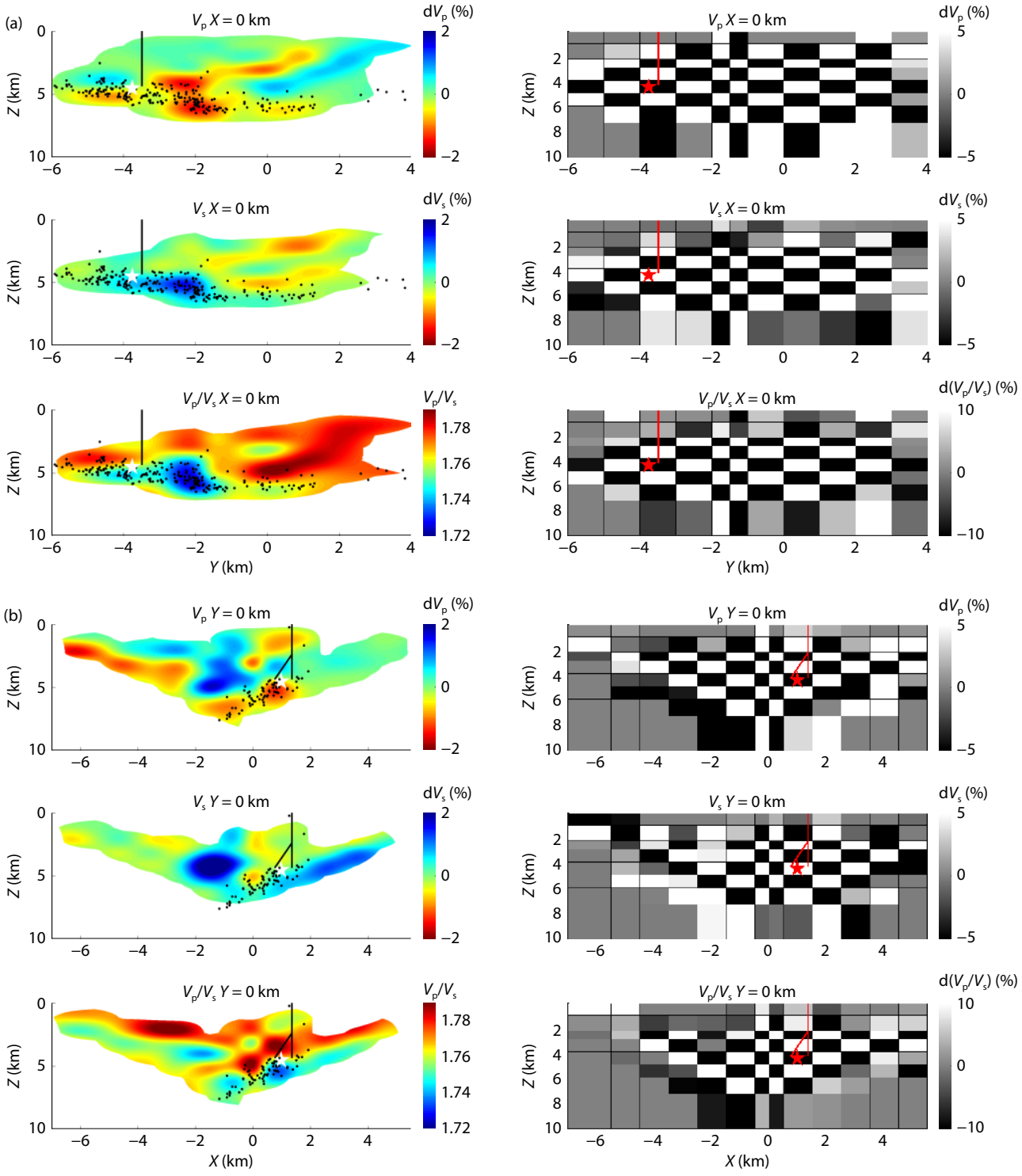

Figure 4. (a) Cross sections of the P-wave velocity perturbation, S-wave velocity perturbation, and V_P/V_S structure at X = 0 km and cross sections of the recovered checkerboard models at X = 0 km. (b) Same as (a) but at Y = 0 km. In the left part of (a) and (b), the black lines are the wells, the black dots are the earthquakes, and the white star is the mainshock; only well resolved areas are shown. In the right part of (a) and (b), the red lines are the wells and the red star is the mainshock.

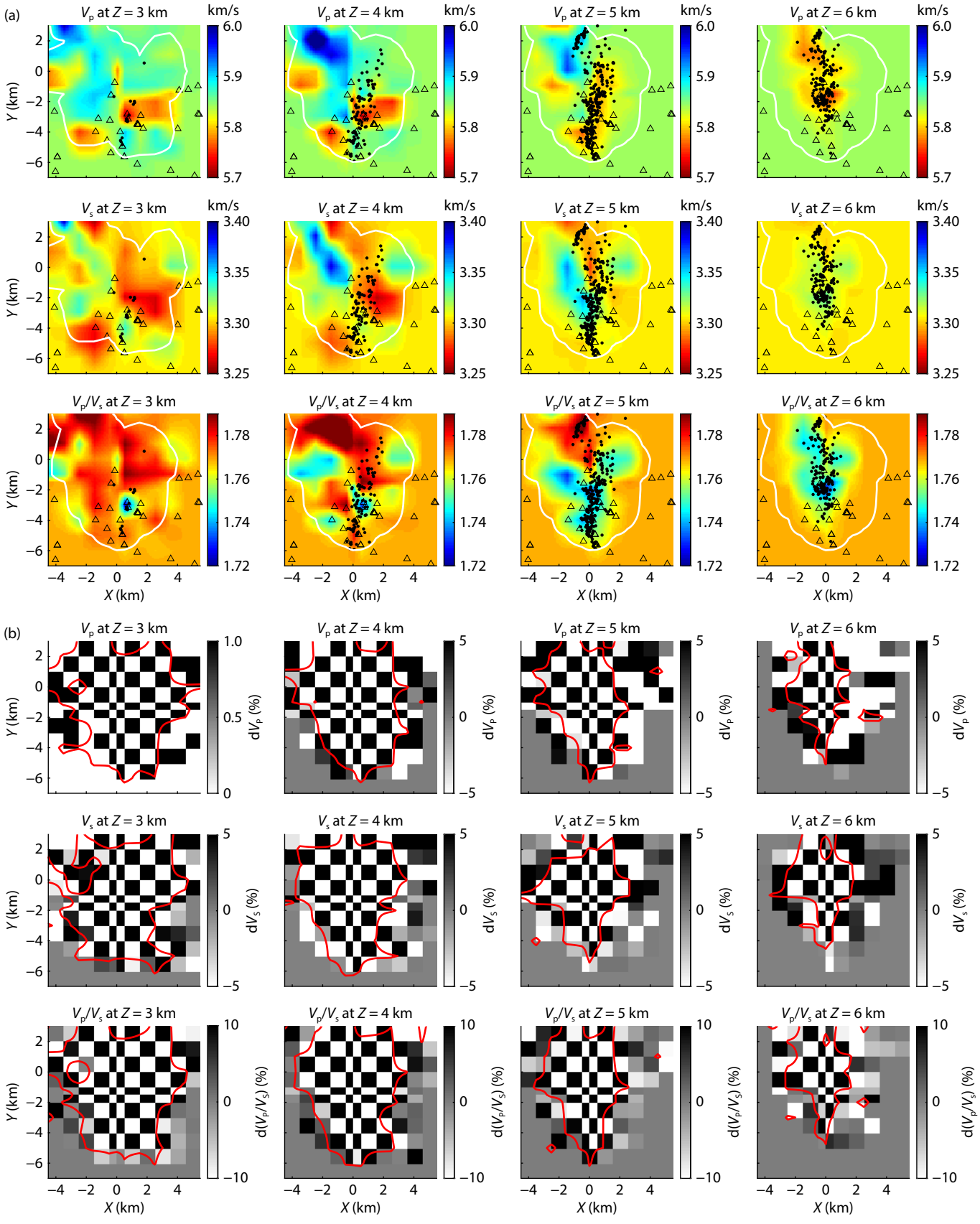

Figure 5. (a) Relocated event distribution maps and V_P, V_S, and V_P/V_S models at different depths. The black dots are the earthquakes projected onto the nearest depth profile. The white lines denote the average DWS values. (b) Recovered results of checkerboard test at different depths. Red contours enclose areas with restoration values greater than 0.85.

from 3 km to 6 km. In order to quantitatively characterize the degree of checkerboard recovery, we adopt a strategy similar to the method proposed by Zelt (1998), where the recovery degree at the *j*th grid node can be defined as by (Guo H et al., 2018)

$$R = \frac{\left(Vt_j + Vr_j\right)^2}{2\left(Vt_j^2 + Vr_j^2\right)}, \tag{3}$$

where Vt_j and Vr_j are the true velocity anomalies and recovered velocity anomalies at the *j*th grid node, respectively. Overall, the aftershock area is well-recovered with recovery values greater than 0.85 (Figure 5b), suggesting that the model resolution is high there. This is because the earthquakes are mainly distributed between 3 and 6 km, so the V_p, V_s, and V_p/V_s checkerboard models are well-recovered in the source region. We also show the well-resolved areas by using the derivative weighted sum (DWS) values. It has been shown that the model regions for which DWS values are greater than the average value are generally well resolved (Zhang H and Thurber, 2007). Figures 4, 5a confirm that model areas with DWS values greater than the average are consistent with the areas of good checkerboard pattern recovery.

From cross sections of V_p, V_s and V_p/V_s models at X = 0 km and Y = 0 km, it can be seen that most of the earthquakes are associated with low V_p (~5.76 km/s), high V_s (~3.34 km/s), and low V_p/V_s (~1.71) anomalies with respect to background values: V_p of ~5.84 km/s, V_s of 3.27 km/s, and V_p/V_s of 1.78 (Figure 4). These features are also clearly observed for depth slices from 5 to 6 km (Figure 5a). In summary, the deep source area of the 2017 M_w5.5 Pohang earthquake is characterized by low V_p, high V_s, and low V_p/V_s anomalies, especially below 4.5 km depth (Figure 6). We also find that, around the depth of 4 km, some aftershocks are associated with relatively low V_s and high V_p/V_s values.

5. Discussions

The deep part of the source region below 4.5 km is characterized by relatively low V_p, high V_s, and low V_p/V_s features. For this EGS site, starting from the depth of 2.35 km, the rock type is granite (Kim et al., 2018). The laboratory experiments show that the V_p/V_s for granite will be increased with pressure and temperature, and can reach 1.75 at the temperature of 100°C and pressure of 350 MPa (Spencer and Nur, 1976). From the Wadati diagram (Wadati and Oki, 1933), the average V_p/V_s for the region of the EGS site from the source region to the surface is 1.76 (Figure 7a). We further estimate the in situ V_p/V_s characteristics of the source region using the method of Lin GQ and Shearer (2007); we find that the in situ V_p/V_s is about 1.7 within the depth range of 4 to 5 km and 1.5 within the depth range of 5 to 6 km (Figure 8). Therefore, the source region where most of aftershocks are located is associated with low V_p/V_s values (Figures 7b).

When granite is fractured and saturated with water, the corresponding V_p/V_s value is generally greater than 1.8 (Wang XQ et al., 2012). However, when fracture aspect ratios are greater (e.g., >0.1), the V_p/V_s ratio could become lower than 1.7 (Takei, 2000, 2002; Brantut and David, 2019). For example, the earthquake source region in Southern California has median in situ V_p/V_s of

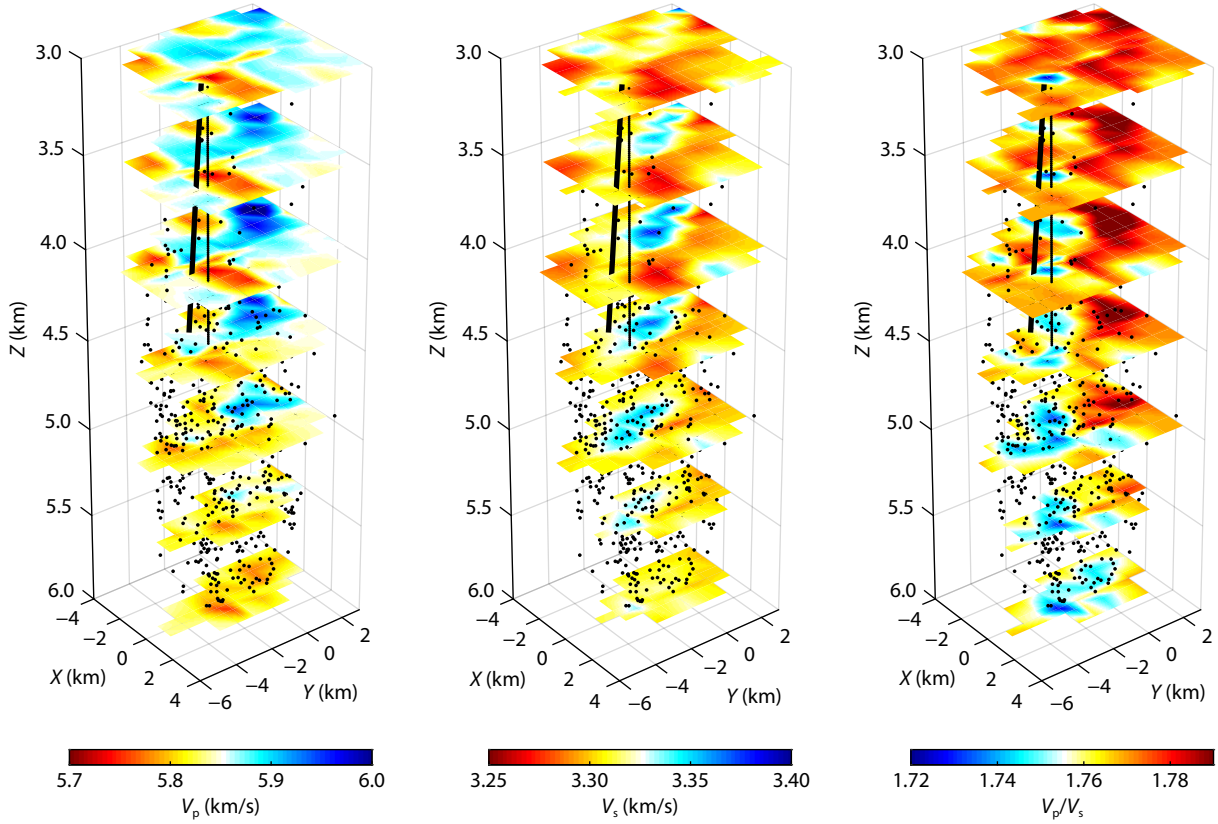

Figure 6. Three-dimensional view of (left) V_p, (middle) V_s, and (right) V_p/V_s models for the depth range of 3 to 6 km. The black lines are the wells and the black dots denote earthquakes.

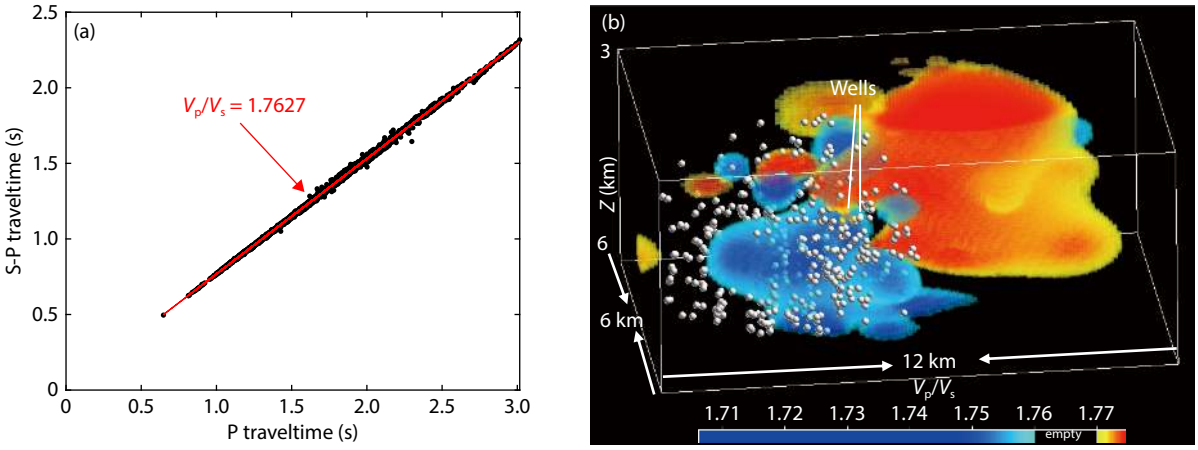

Figure 7. (a) Average V_p/V_s ratio in the Pohang EGS site via the Wadati method. (b) 3D distribution of relative higher velocity ratios (red, >1.77) and lower velocity ratios (blue, <1.76) sculpted from the inverted V_p/V_s model shown in Figure 6. The white dots are the earthquakes.

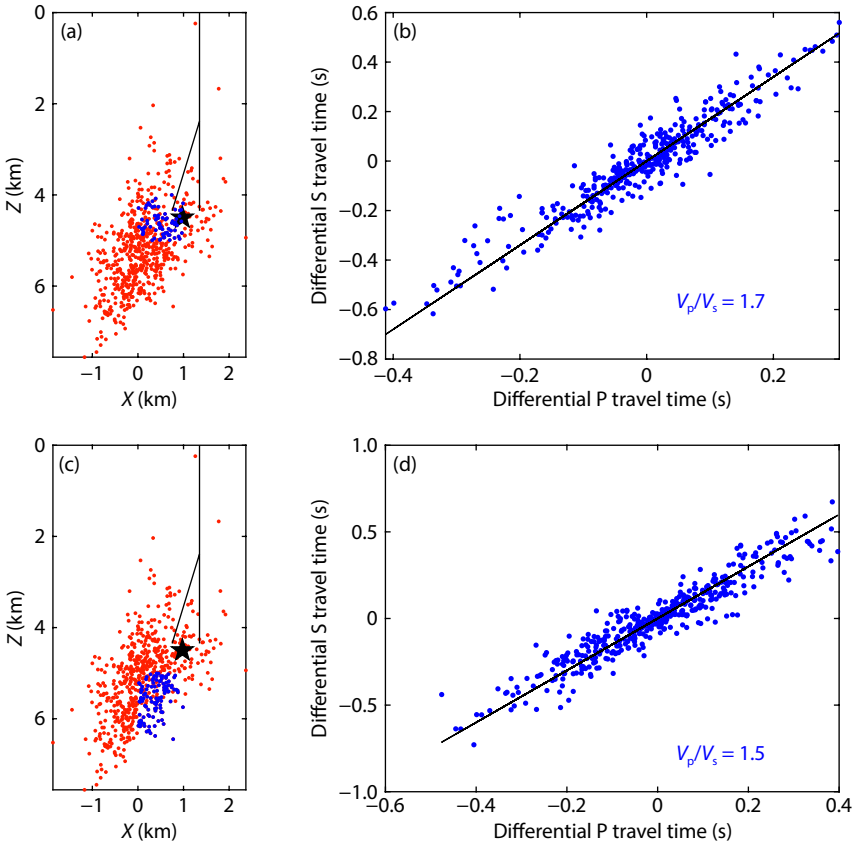

Figure 8. Vertical cross-section view of in-situ V_p/V_s ratios. The blue dots in (b) and (d) indicate the differential P and S arrival times. The slopes of the lines are the local V_p/V_s ratio (Lin GQ and Shearer, 2007). In (a) and (c), red dots represent all earthquakes and blue dots represent the earthquakes used for estimating in-situ V_p/V_s ratios in (b) and (d) respectively.

about 1.67 (Lin GQ and Shearer, 2009). However, no matter how the aspect ratios change, fluid-filled cracks generally cause lower V_s values (Takei, 2000, 2002), which is not consistent with the high V_s anomalies imaged in the Pohang earthquake source region. Therefore, our observed low V_p/V_s values in the deep source region of the 2017 Pohang earthquake cannot be explained just by fluid-filled cracks.

Low V_p/V_s ratios have been observed along the fissure swarm; they have been interpreted as a product of supercritical fluids (Foulger et al., 1995). Any fluid at a temperature and pressure beyond the critical point is a supercritical fluid. The critical point of water is at 374°C and 22.1 MPa (Sánchez-Pastor et al., 2021). Assessment of geothermal resources in south Korea have found that the temperature at 5 km depth in the Pohang area is expected to be about 180°C (Lee et al., 2010), where the geothermal gradient is ~30 °C/km (Lee et al., 2011). Therefore, at the source region, liquids could not reach a critical state because of low

temperatures; thus, our observed low V_p/V_s anomalies cannot be due to supercritical fluids.

When the temperature is high, as long as the pressure is not very high, the fluids will be in the vapor state (Figure 9). At the depth of 4278 m near the wells, the maximum, intermediate, and minimum principal stresses are 139, 110, and 82 MPa, respectively (Hofmann et al., 2019). In comparison, the maximum recorded wellhead pressure at PX-1 was 27.2 MPa, and the maximum wellhead pressure at PX-2 was 89.2 MPa (Terakawa et al., 2020). Thus in the Pohang earthquake source region, the occurrence of the earthquake is associated with relatively low pressure conditions. Therefore, it is possible that the source region of the 2017 Pohang earthquake was not only filled with overpressurized fluids (Terakawa et al., 2020) but also that these fluids were most likely in a vapor state in the deep area below 4.5 km depth. The lab experiments showed that vapor-dominated pore spaces can increase the S-wave velocity (Toksöz et al., 1976), and decrease V_p/V_s ratios (Wang XQ et al., 2012). This is consistent with our observations of high V_s and low V_p/V_s values. The mechanisms currently proposed to explain how injected fluids can induce earthquakes mainly assume that the fluids are in the liquid state (Schultz et al., 2020). Our tomography results suggest that the vapor state can also play a role in inducing earthquakes and should also be considered.

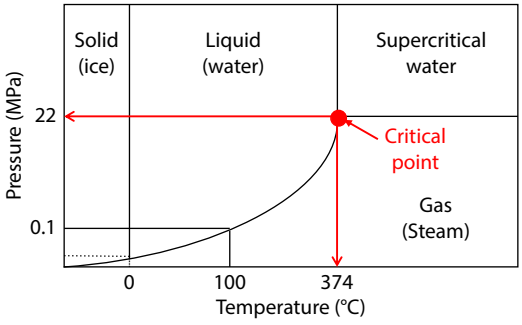

Figure 9. The phase diagram of water (adapted from Sánchez-Pastor et al., 2021).

Around the depth of 4 km, some aftershocks are associated with relatively low V_s and high V_p/V_s values. This could be because, at this depth, the fluids have not reached the steam state. Thus, the liquid-dominated cracks cause relatively low V_s and high V_p/V_s values. As the depth increases, the temperatures increase, and the injected/leaked fluids start to be in the steam state so that the vapor-adominated cracks lead to the decrease of the V_p/V_s ratios.

Low V_p/V_s ratios have also been observed in hydrothermal areas. For example, in the Geysers geothermal field, low V_p/V_s ratios were observed and interpreted to be caused by a pressure drop of 1 MPa in the steam filled pores from 1991 to 1994 (Julian et al., 1996, Foulger et al., 1997, Gritto and Jarpe, 2014). Similarly, for the source region of the Pohang earthquake, decreased pressure in the vapor-dominated pore spaces in the source area after the main shock rupture could also contribute to low V_p/V_s ratios observed there.

In this study, in addition to determining the velocity structures of the source area, we also simultaneously determined earthquake locations, including that of the main shock of the 2017 Pohang earthquake. The RMS travel time residual for the mainshock is 19 ms, indicating it is well relocated. In general, an earthquake's aftershock distribution can be used to delineate the coseismic slip area or the asperity of the mainshock. Previous studies have found that the initiation point of the mainshock is located at the edge of the asperity or the main coseismic slip area (Liu X and Zhao DP, 2018; Li JL et al., 2023). It is also generally accepted that an increase in pore pressures near the asperity (or the strong part along the fault plane) can facilitate initiation of a mainshock. For the Pohang earthquake, we find, as expected, that the mainshock is located around the edge of the aftershock area. Overall, our velocity images further support the hypothesis that the occurrence of the 2017 Pohang earthquake was caused by reactivation of a blind fault due to fluid injections (Choi et al., 2019; Woo et al., 2019).

6. Conclusions

In this study, we have created high-resolution 3D V_p, V_s and V_p/V_s structures for the source area of the 2017 Pohang earthquake by applying a V_p/V_s model consistency-constrained double-difference seismic tomography method to the earthquake data recorded between 15 November 2017 and 20 February 2018 by a local seismic network. We find that the depth of the mainshock was about 4.5 km, very close to the two exploratory wells. The activated fault, delineated by aftershocks, extends to a depth of 7 km. Aftershocks of the M_w5.5 Pohang earthquake were located mainly in a region with relatively high V_s and low V_p/V_s values, which can be interpreted as due to overpressured vapors. Our study shows that obtaining detailed velocity structures, especially V_p/V_s ratios, can help to understand the seismogenic mechanisms of an earthquake. The velocity images presented here support the inference that the 2017 Pohang earthquake was is triggered by an increase of pore pressures near its asperity caused by migration of injected fluids into a blind fault.

Acknowledgments

We are very grateful for constructive comments from two anonymous reviewers that were very helpful in improving the original manuscript. This work was supported by the National Natural Science Foundation of China (42304056) and the Natural Science Foundation of Hebei Province (D2023305007). This work was also supported by the Basic Research Project (GP2020-017, GP2020-027) of the Korea Institute of Geoscience and Mineral Resources (KIGAM) funded by the Ministry of Science and ICT of Korea. We are grateful for Luanxiao Zhao for insightful discussions on supercritical fluids.

References

Anderson, A., and Rezaie, B. (2019). Geothermal technology: Trends and potential role in a sustainable future. *Appl. Energy*, *248*, 18–34. https://doi.org/10.1016/j.apenergy.2019.04.102

Anyiam, U. O., Zhang, H. J., Tan, Y. Y., Qian, J. W., Gao, L., Liu, Y., Zuo, K. Z., and Zhao, C. P. (2023). Enhanced 3D velocity structure, seismicity relocation and basement characterization of Changning shale gas and salt mining regions in southern Sichuan basin. *Front. Earth Sci.*, *10*, 1082122. https://doi.org/10.3389/feart.2022.1082122

Bhattacharya, P., and Viesca, R. C. (2019). Fluid-induced aseismic fault slip

outpaces pore-fluid migration. *Science*, *364*(6439), 464–468. https://doi.org/10.1126/science.aaw7354

Brantut, N., and David, E. C. (2019). Influence of fluids on V_P/V_S ratio: Increase or decrease?. *Geophys. J. Int.*, *216*(3), 2037–2043. https://doi.org/10.1093/gji/ggy518

Cao, Y., Jin, M. P., Qian, J. W., Chen, J., and Anyiam, U. O. (2023). Crustal structure and seismicity characteristics based on dense array monitoring in northwestern Yunnan, China. *Phys. Earth Planet. Inter.*, *340*, 107047. https://doi.org/10.1016/j.pepi.2023.107047

Charléty, J., Cuenot, N., Dorbath, L., Dorbath, C., Haessler, H., and Frogneux, M. (2007). Large earthquakes during hydraulic stimulations at the geothermal site of Soultz-sous-Forêts. *Int. J. Rock Mech. Min. Sci.*, *44*(8), 1091–1105. https://doi.org/10.1016/j.ijrmms.2007.06.003

Choi, J. H., Ko, K., Gihm, Y. S., Cho, C. S., Lee, H., Song, S. G., Bang, E. S., Lee, H. J., Bae, H. K., ... Lee, S. R. (2019). Surface deformations and rupture processes associated with the 2017 M_W 5.4 Pohang, Korea, earthquake. *Bull. Seismol. Soc. Am.*, *109*(2), 756–769. https://doi.org/10.1785/0120180167

Christensen, N. I. (1996). Poisson's ratio and crustal seismology. *J. Geophys. Res.: Solid Earth*, *101*(B2), 3139–3156. https://doi.org/10.1029/95JB03446

Concha, D., Fehler, M., Zhang, H. J., and Wang, P. (2010). Imaging of the Soultz enhanced geothermal reservoir using microseismic data. In *Proceedings Thirty-Fifth Workshop on Geothermal Reservoir Engineering*. Stanford, USA: Stanford University.

Ellsworth, W. L. (2013). Injection-induced earthquakes. *Science*, *341*(6142), 1225942. https://doi.org/10.1126/science.1225942

Ellsworth, W. L., Giardini, D., Townend, J., Ge, S. M., and Shimamoto, T. (2019). Triggering of the Pohang, Korea, earthquake (M_W 5.5) by enhanced geothermal system stimulation. *Seismol. Res. Lett.*, *90*(5), 1844–1858. https://doi.org/10.1785/0220190102

Evans, K. F., Zappone, A., Kraft, T., Deichmann, N., and Moia, F. (2012). A survey of the induced seismic responses to fluid injection in geothermal and CO_2 reservoirs in Europe. *Geothermics*, *41*, 30–54. https://doi.org/10.1016/j.geothermics.2011.08.002

Foulger, G. R., Miller, A. D., Julian, B. R., and Evans, J. R. (1995). Three-dimensional υ_p and υ_p/υ_s structure of the Hengill Triple Junction and Geothermal Area, Iceland, and the repeatability of tomographic inversion. *Geophys. Res. Lett.*, *22*(10), 1309–1312. https://doi.org/10.1029/94GL03387

Foulger, G. R., Grant, C. C., Ross, A., and Julian, B. R. (1997). Industrially induced changes in Earth structure at the geysers geothermal area, California. *Geophys. Res. Lett.*, *24*(2), 135–137. https://doi.org/10.1029/96GL03152

Grigoli, F., Cesca, S., Rinaldi, A. P., Manconi, A., López-Comino, J. A., Clinton, J. F., Westaway, R., Cauzzi, C., Dahm, T., Wiemer, S. (2018). The November 2017 M_W 5.5 Pohang earthquake: A possible case of induced seismicity in South Korea. *Science*, *360*(6392), 1003–1006. https://doi.org/10.1126/science.aat2010

Gritto, R., and Jarpe, S. P. (2014). Temporal variations of V_p/V_s-ratio at The Geysers geothermal field, USA. *Geothermics*, *52*, 112–119. https://doi.org/10.1016/j.geothermics.2014.01.012

Guo, H., Zhang, H. J., and Froment, B. (2018). Structural control on earthquake behaviors revealed by high-resolution V_p/V_s imaging along the Gofar transform fault, East Pacific Rise. *Earth Planet. Sci. Lett.*, *499*, 243–255. https://doi.org/10.1016/j.epsl.2018.07.037

Häring, M. O., Schanz, U., Ladner, F., and Dyer, B. C. (2008). Characterisation of the Basel 1 enhanced geothermal system. *Geothermics*, *37*(5), 469–495. https://doi.org/10.1016/j.geothermics.2008.06.002

Hofmann, H., Zimmermann, G., Farkas, M., Huenges, E., Zang, A., Leonhardt, M., Kwiatek, G., Martinez-Garzon, P., Bohnhoff, M., ... Kim, K. Y. (2019). First field application of cyclic soft stimulation at the Pohang Enhanced Geothermal System site in Korea. *Geophys. J. Int.*, *217*(2), 926–949. https://doi.org/10.1093/gji/ggz058

Julian, B. R., Ross, A., Foulger, G. R., and Evans, J. R. (1996). Three-dimensional seismic image of a geothermal reservoir: The Geysers, California. *Geophys. Res. Lett.*, *23*(6), 685–688. https://doi.org/10.1029/95GL03321

Kim, K. H., Ree, J. H., Kim, Y., Kim, S., Kang, S. Y., and Seo, W. (2018). Assessing whether the 2017 M_W 5.4 Pohang earthquake in South Korea was an induced event. *Science*, *360*(6392), 1007–1009. https://doi.org/10.1126/science.aat6081

Kim, K. H., Seo, W., Han, J., Kwon, J., Kang, S. Y., Ree, J. H., Kim, S., and Liu, K. (2020). The 2017 M_L 5.4 Pohang earthquake sequence, Korea, recorded by a dense seismic network. *Tectonophysics*, *774*, 228306. https://doi.org/10.1016/j.tecto.2019.228306

Lee, K. K., Ellsworth, W. L., Giardini, D., Townend, J., Ge, S. M., Shimamoto, T., Yeo, I. W., Kang, T. S., Rhie, J., ... Langenbruch, C. (2019). Managing injection-induced seismic risks. *Science*, *364*(6442), 730–732. https://doi.org/10.1126/science.aax1878

Lee, T. J., Song, Y., Yoon, W. S., Kim, K. Y., Jeon, J., Min, K. B., and Cho, Y. H. (2011). The first enhanced geothermal system project in Korea. Ibusuki, Japan: In *Proceedings of the 9th Asian Geothermal Symposium* (pp. 129-132).

Lee, Y., Park, S., Kim, J., Kim, H. C., and Koo, M. H. (2010). Geothermal resource assessment in Korea. *Renew. Sustain. Energy Rev.*, *14*(8), 2392–2400. https://doi.org/10.1016/j.rser.2010.05.003

Lei, X. L., Wang, Z. W., and Su, J. R. (2019). Possible link between long-term and short-term water injections and earthquakes in salt mine and shale gas site in Changning, south Sichuan Basin, China. *Earth Planet. Phys.*, *3*(6), 510–525 https://doi.org/10.26464/epp2019052

Li, J. L., Xu, J., Zhang, H. J., Yang, W., Tan, Y. Y., Zhang, F. S., Meng, L. Y., Zang, Y., Miao, S. Y., ... Sun, J. B. (2023). High seismic velocity structures control moderate to strong induced earthquake behaviors by shale gas development. *Commun. Earth Environ.*, *4*(1), 188. https://doi.org/10.1038/s43247-023-00854-x

Lin, G. Q., and Shearer, P. (2007). Estimating local V_p/V_s ratios within similar earthquake clusters. *Bull. Seismol. Soc. Am.*, *97*(2), 379–388. https://doi.org/10.1785/0120060115

Lin, G. Q., and Shearer, P. M. (2009). Evidence for water-filled cracks in earthquake source regions. *Geophys. Res. Lett.*, *36*(17), L17315. https://doi.org/10.1029/2009GL039098

Lin, G. Q., and Wu, B. (2018). Seismic velocity structure and characteristics of induced seismicity at the Geysers geothermal field, eastern California. *Geothermics*, *71*, 225–233. https://doi.org/10.1016/j.geothermics.2017.10.003

Liu, H. Y., Peng, C., Xue, L. F., Li, W. Q., Xu, C. H., and Jofrisse, C. S. (2022). Non-seismic geophysical analysis of potential geothermal resources in the Longgang Block, Northeast China. *Earth Planet. Phys.*, *6*(6), 576–591. https://doi.org/10.26464/epp2022046

Liu, X., and Zhao, D. P. (2018). Upper and lower plate controls on the great 2011 Tohoku-oki earthquake. *Sci. Adv.*, *4*(6), eaat4396. https://doi.org/10.1126/sciadv.aat4396

Lu, S. M. (2018). A global review of enhanced geothermal system (EGS). *Renew. Sustain. Energy Rev.*, *81*, 2902–2921. https://doi.org/10.1016/j.rser.2017.06.097

Olasolo, P., Juárez, M. C., Morales, M. P., D'Amico, S., and Liarte, I. A. (2016). Enhanced geothermal systems (EGS): A review. *Renew. Sustain. Energy Rev.*, *56*, 133–144. https://doi.org/10.1016/j.rser.2015.11.031

Sánchez-Pastor, P., Obermann, A., Reinsch, T., Ágústsdóttir, T., Gunnarsson, G., Tómasdóttir, S., Hjörleifsdóttir, V., Hersir, G. P., Ágústsson, K., and Wiemer, S. (2021). Imaging high-temperature geothermal reservoirs with ambient seismic noise tomography, a case study of the Hengill geothermal field, SW Iceland. *Geothermics*, *96*, 102207. https://doi.org/10.1016/j.geothermics.2021.102207

Schultz, R., Skoumal, R. J., Brudzinski, M. R., Eaton, D., Baptie, B., and Ellsworth, W. (2020). Hydraulic fracturing-induced seismicity. *Rev. Geophys.*, *58*(3), e2019RG000695. https://doi.org/10.1029/2019RG000695

Spencer, Jr. J. W., and Nur, A. M. (1976). The effects of pressure, temperature, and pore water on velocities in Westerly granite. *J. Geophys. Res.*, *81*(5), 899–904. https://doi.org/10.1029/JB081i005p00899

Takei, Y. (2000). Acoustic properties of partially molten media studied on a simple binary system with a controllable dihedral angle. *J. Geophys. Res.: Solid Earth*, *105*(B7), 16665–16682. https://doi.org/10.1029/2000JB900124

Takei, Y. (2002). Effect of pore geometry on V_P/V_S: From equilibrium geometry to crack. *J. Geophys. Res.: Solid Earth*, *107*(B2), 2043. https://doi.org/10.1029/

2001jb000522

Tan, Y. Y., Hu, J., Zhang, H. J., Chen, Y. K., Qian, J. W., Wang, Q. F., Zha, H. S., Tang, P., and Nie, Z. (2020). Hydraulic fracturing induced seismicity in the southern Sichuan Basin due to fluid diffusion inferred from seismic and injection data analysis. *Geophys. Res. Lett.*, *47*(4), e2019GL084885. https://doi.org/10.1029/2019GL084885

Tan, Y. Y., Qian, J. W., Hu, J., Zhang, H. J., Xing, H. L., Li, J. L., Xu, J., Yang, W., Gu, N., and Miao, S. Y. (2023). Tomographic evidences for hydraulic fracturing induced seismicity in the Changning shale gas field, southern Sichuan Basin, China. *Earth Planet. Sci. Lett.*, *605*, 118021. https://doi.org/10.1016/j.epsl.2023.118021

Terakawa, T., Seo, W., Kim, K. H., and Ree, J. H. (2020). Three-dimensional pore fluid pressures in source region of 2017 Pohang earthquake inferred from earthquake focal mechanisms. *Geophys. Res. Lett.*, *47*(9), e2019GL085964. https://doi.org/10.1029/2019GL085964

Thurber, C. (1993). Local earthquake tomography: Velocities and Vp/Vs-theory. In: H. M. Iyer, et al. (Eds.), *Seismic Tomography: Theory and Practice* (pp. 563-583). London: Chapman & Hall.

Toksöz, M. N., Cheng, C. H., and Timur, A. (1976). Velocities of seismic waves in porous rocks. *Geophysics*, *41*(4), 621–645. https://doi.org/10.1190/1.1440639

Wadati, K., and Oki, S. (1933). On the travel time of earthquake waves. (Part II). *J. Meteor. Soc. Japan Ser II*, *11*(1), 14–28.

Waldhauser, F., and Ellsworth, W. L. (2000). A double-difference earthquake location algorithm: Method and application to the northern Hayward fault, California. *Bull. Seismol. Soc. Am.*, *90*(6), 1353–1368. https://doi.org/10.1785/0120000006

Wang, X. Q., Schubnel, A., Fortin, J., David, E. C., Guéguen, Y., and Ge, H. K. (2012). High Vp/Vs ratio: saturated cracks or anisotropy effects?. *Geophys. Res. Lett.*, *39*(11), L11307. https://doi.org/10.1029/2012GL051742

Wong, W. C. J., Zi, J. P., Yang, H. F., and Su, J. R. (2021). Spatial-temporal evolution of injection-induced earthquakes in the Weiyuan Area determined by machine-learning phase picker and waveform cross-correlation. *Earth Planet. Phys.*, *5*(6), 485–500 https://doi.org/10.26464/epp2021055

Woo, J. U., Kim, M., Sheen, D. H., Kang, T. S., Rhie, J., Grigoli, F., Ellsworth, W. L., and Giardini, D. (2019). An in-depth seismological analysis revealing a causal link between the 2017 M_w 5.5 Pohang earthquake and EGS project. *J. Geophys. Res.: Solid Earth*, *124*(12), 13060–13078. https://doi.org/10.1029/2019JB018368

Yeo, I. W., Brown, M. R. M., Ge, S., and Lee, K. K. (2020). Causal mechanism of injection-induced earthquakes through the M_W 5.5 Pohang earthquake case study. *Nat. Commun.*, *11*(1), 2614. https://doi.org/10.1038/s41467-020-16408-0

Yin, X. X., Jiang, C. S., Zhai, H. Y., Zhang, Y. B., Jiang, C., Lai, G. J., Zhu, A. Y., and Yin, F. L. (2021). Review of induced seismicity and disaster risk control in dry hot rock resource development worldwide. *Chin. J. Geophys. (in Chinese)*, *64*(11), 3817–3836. https://doi.org/10.6038/cjg2021O0448

Yoo, H., Park, S., Xie, L. M., Kim, K. I., Min, K. B., Rutqvist, J., and Rinaldi, A. P. (2021). Hydro-mechanical modeling of the first and second hydraulic stimulations in a fractured geothermal reservoir in Pohang, South Korea. *Geothermics*, *89*, 101982. https://doi.org/10.1016/j.geothermics.2020.101982

Zelt, C. A. (1998). Lateral velocity resolution from three-dimensional seismic refraction data. *Geophys. J. Int.*, *135*(3), 1101–1112. https://doi.org/10.1046/j.1365-246X.1998.00695.x

Zhang, H., and Thurber, C. H. (2007). Estimating the model resolution matrix for large seismic tomography problems based on Lanczos bidiagonalization with partial reorthogonalization. *Geophys. J. Int.*, *170*(1), 337–345. https://doi.org/10.1111/j.1365-246X.2007.03418.x

Zhang, H. J., and Thurber, C. H. (2003). Double-difference tomography: the method and its application to the Hayward fault, California. *Bull. Seismol. Soc. Am.*, *93*(5), 1875–1889. https://doi.org/10.1785/0120020190

Zhang, H. J., Thurber, C., and Bedrosian, P. (2009). Joint inversion for Vp, Vs, and Vp/Vs at SAFOD, Parkfield, California. *Geochem. Geophys. Geosyst.*, *10*(11), Q11002. https://doi.org/10.1029/2009GC002709

Zuo, K. Z., Zhao, C. P., and Zhang, H. J. (2020). 3D crustal structure and seismicity characteristics of Changning–Xingwen area in the southwestern Sichuan basin, China. *Bull. Seismol. Soc. Am.*, *110*(5), 2154–2167. https://doi.org/10.1785/0120200085